VEHICLE SYSTEM DYNAMICS
https://doi.org/10.1080/00423114.2025.2505619

Optimising vehicle performance with advanced active aerodynamic systems

Steven Rijns [a], Tom-Robin Teschner [b], Kim Blackburn [a], Efstathios Siampis [a] and James Brighton [a]

[a]Advanced Vehicle Engineering Centre, Cranfield University, Cranfield, UK; [b]Centre for Computational Engineering Sciences, Cranfield University, Cranfield, UK

ABSTRACT

This study investigates the performance potential of advanced active aerodynamic systems on high-performance vehicles. Static and active aerodynamic configurations, including asymmetrically actuated systems, are evaluated to identify performance gains and the mechanisms driving these improvements. Vehicle performance is optimised using a minimum lap time simulation framework, which utilises a transient vehicle dynamics model and CFD-derived aerodynamic data. Results indicate that configurations with greater aerodynamic adaptability enhance acceleration, braking, cornering, and straight-line performance, yielding notable lap time reductions compared to a static aerodynamic configuration. The asymmetrically controlled aerodynamic configuration achieves the highest lap time reduction of approximately 0.92 s (0.76%) due to its ability to modulate downforce both longitudinally and laterally. Optimal control strategies show that aerodynamic elements are actuated to balance vertical tyre load shifts resulting from load transfer, prioritising downforce on underloaded tyres in demanding scenarios like braking, cornering, and acceleration. Additionally, optimal design parameters for the brake, torque and roll stiffness distributions shift rearward as configurations provide greater control of aerodynamic loads on the rear axle. Overall, this research demonstrates the performance advantages of active aerodynamic systems and offers insights into the mechanisms underlying these enhancements, establishing a foundation for further innovations in the field.

ARTICLE HISTORY
Received 17 November 2024
Revised 3 April 2025
Accepted 6 May 2025

KEYWORDS
Active aerodynamics; performance optimisation; minimum lap time; optimal control; vehicle dynamics; computation fluid dynamics

1. Introduction

The pursuit of greater efficiency and performance continues to drive advancements in the automotive industry, especially within motorsport and high-performance vehicle sectors. Recently, active aerodynamic systems, which can dynamically adapt to a vehicle's operating condition, have gained significant attention, highlighted by the upcoming introduction of active aerodynamics in Formula One in 2026 [1]. Such innovations not only have the

CONTACT Steven Rijns steven.rijns@cranfield.ac.uk

This article has been corrected with minor changes. These changes do not impact the academic content of the article.

potential to provide a competitive edge on the track, but also pave the way for future trends in automotive engineering.

This study explores the performance potential of advanced active aerodynamic systems on high-performance vehicles. It evaluates static and active aerodynamic setups, including a configuration with asymmetric aerodynamic control capabilities, to determine performance enhancements and the underlying mechanisms driving these gains. The vehicle performance of each aerodynamic configuration is optimised using a comprehensive simulation framework, based on a detailed vehicle dynamics model and representative aerodynamic data, which minimises lap time by optimising the vehicle's trajectory, control inputs, and parameter combinations.

The performance analyses of various aerodynamic configurations require coupling of the vehicle's aerodynamics and dynamics. Among commonly used methods, quasi-steady static coupling, which utilises data from steady-state Computational Fluid Dynamics (CFD) simulations, is generally considered the most cost-effective for studies on passenger-sized vehicles [2–5]. This is also reflected by research on the influence of aerodynamic systems on vehicle handling, which predominantly use quasi-steady static coupling.

In these studies, aerodynamic devices positioned near a vehicle's front and rear axles have been shown to influence understeer and oversteer behaviour, thereby enhancing stability during dynamic manoeuvres [6,7]. When combined with an effective control strategy that balances aerodynamic loads according to mechanical grip, these systems can reduce lap times by approximately 3% [8]. Additionally, research on rear wings functioning as air brakes has demonstrated improvements in stability during braking events and reductions in braking distance by over 6%, particularly at higher speeds [9–11].

Research on asymmetric active aerodynamic systems has also shown promising results. Studies on split wings, which can vary the angle of attack between the left- and right-side elements, have demonstrated lateral downforce variations of 25%–60%, depending on the wing design [12,13]. By prioritising downforce on the inside tyres during cornering, these systems enhance lateral stability during evasive manoeuvres, improve cornering velocity, and reduce lap times when paired with an effective control strategy [14–17]. These improvements are more pronounced at higher speeds and are further enhanced by an effective longitudinal downforce distribution.

Further research on asymmetric active aerodynamic systems has highlighted the potential of tilt wings, which can laterally redistribute downforce and introduce a centripetal force [18]. Road tests have shown that vehicles with tilt rear wings can achieve a 13% higher cornering velocity compared to those without aerodynamic devices [19]. Additionally, a comparative study found that split and tilt wings increased cornering velocity by 0.5% and 2%, respectively, compared to conventional symmetric high downforce setups. The tilt wing outperformed the split rear wing due to its greater ability to influence vertical tyre loads, introduce a centripetal force, and provide a more consistent response to control strategies [20].

The studies reviewed above mainly relied on steady-state limit handling analyses in specific driving scenarios to investigate the impact of aerodynamic systems on vehicle performance. Other research has employed minimum lap time simulations, formulated as an Optimal Control Problem (OCP), aimed at minimising lap time by optimising control inputs while adhering to track constraints and vehicle performance limits [21,22]. Such simulations provide a comprehensive view of vehicle performance, offering detailed

insights into optimal driver inputs, racing lines, control of active systems, and vehicle design parameters.

Previous research has effectively utilised minimum lap time simulations with varying complexities in trajectory planning and dynamics modelling to evaluate vehicle performance [23–27]. Findings on conventional aerodynamics have indicated that lap times can vary by nearly 2% depending on the aerodynamic balance position, with a hypothetical variable aerodynamic balance offering an approximate 0.3% improvement over an optimised static balance [28,29]. Studies on static and active aerodynamic systems, combined with various propulsion configurations, have demonstrated lap time improvements of about 0.7%–1% and showed how the aerodynamic systems were actuated to achieve these enhancements [30,31].

The literature highlights the potential of active aerodynamic systems to enhance vehicle performance, particularly in braking, cornering, and stability. However, existing research has largely relied on steady-state limit handling analyses, minimum lap time simulations with fixed-trajectory planning or quasi-steady-state dynamics, and simplified aerodynamic models. This leaves a significant gap in understanding the performance potential and underlying mechanisms driving the enhancements of more advanced active aerodynamic systems on high-performance vehicles, especially through a comprehensive free-trajectory and transient dynamics minimum lap time simulation approach.

This study addresses this research gap by analysing the performance of various static and active aerodynamic configurations, including a configuration with asymmetric aerodynamic control capabilities, designed to influence downforce distribution both longitudinally and laterally. The performance of each aerodynamic configuration is reflected by a lap around the Circuit de Barcelona-Catalunya, which encompasses a wide range of driving scenarios. Vehicle performance is optimised through a lap time simulation framework that leverages a detailed vehicle dynamics model and CFD-derived aerodynamic data, aiming to minimise lap time by simultaneously optimising the vehicle's trajectory, control inputs, and parameter combinations. Through comprehensive investigations, this research provides detailed insights into the performance gains provided by the active aerodynamic systems, their optimal control to realise these enhancements, and shifts in optimised design parameters in response to these systems.

2. Vehicle configurations

This study utilises an advanced high-performance vehicle concept, based on the *DrivAer hp-F* [32], a high-performance variant of the DrivAer Fastback automotive reference model [33]. This advanced high-performance vehicle concept, as introduced by Rijns et al. [20], has forebody strakes, a smooth underbody, a 10° multichannel diffuser, and is equipped with an active split front wing and tilt rear wing. The left and right front wing elements can vary their angle of attack between 0° and 10°. The rear wing can adjust its angle of attack between 0° and 30°, and its tilt angle by ± 12°. The high-performance vehicle concept is illustrated in Figure 1 and its main dimensions are listed in Table 1.

Four aerodynamic configurations, each based on this vehicle geometry, are examined to assess the impact of varying levels of aerodynamic adaptability on vehicle performance. The first configuration is classified as 'static', featuring a front and rear wing with fixed angular settings, which serves as a baseline for comparison. The second configuration

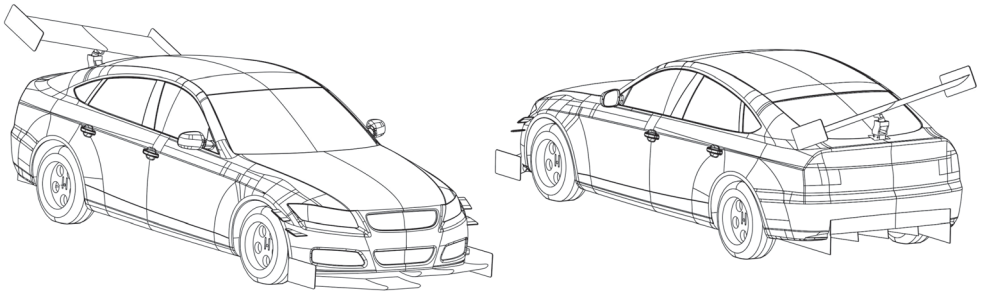

Figure 1. Advanced high-performance vehicle concept featuring an active split front wing and active tilt rear wing. The aerodynamic systems are displayed in an asymmetric operating setting to illustrate the design.

maintains a fixed front wing angle while introducing active control over the rear wing angle, whereas the third configuration enables active control over both the front and rear wing angles. Through these capabilities, the second and third configurations influence aerodynamic balance longitudinally. Finally, the fourth configuration allows independent active control of the left and right front wing angles, as well as active control of the rear wing's angle of attack and tilt angle. This asymmetric actuation functionality enables modulation of the aerodynamic balance both longitudinally and laterally, which is therefore classified as an 'advanced active' aerodynamic system.

Table 1. Vehicle parameters.

Parameter	Value	Unit	Description
L	4.613	m	Length
W	1.792	m	Width
H	1.397	m	Height
A_{ref}	2.160	m^2	Frontal area
h_0	0.130	m	Ride height
m	1565	kg	Total mass
m_s	1375	kg	Sprung mass
$m_{u,f}$	90	kg	Front unsprung mass
$m_{u,r}$	100	kg	Rear unsprung mass
I_z	1450	kg m^2	Yaw moment of inertia
l	2.786	m	Wheelbase
l_f	1.393	m	Distance between front axle and COG
l_r	1.393	m	Distance between rear axle and COG
t_w	1.520	m	Track width
h_{COG}	0.500	m	Height of COG
$h_{u,f}$	0.297	m	Height of front unsprung mass
$h_{u,r}$	0.297	m	Height of rear unsprung mass
h_f	0.070	m	Height of front roll centre
h_r	0.110	m	Height of rear roll centre
h_{RW}	1.280	m	Height of rear wing
d	0.410	m	Distance between COG and roll axis
R_w	0.314	m	Wheel radius
I_w	0.9	kg m^2	Wheel rotational inertia
k_ϕ	1.146×10^5	Nm/rad	Total roll stiffness
$P_{e,\max}$	456	kW	Maximum electric motor power
$T_{e,\max}$	602	Nm	Maximum electric motor torque
$\Omega_{e,\max}$	17750	RPM	Maximum electric motor speed
γ_g	7.252	–	Final gear ratio

3. Aerodynamic performance simulations

The vehicle's aerodynamic performance data is obtained through CFD simulations, which adopt the authors' well-established methodology used in [20,34]. This methodology is founded on a comprehensive grid convergence study, turbulence model evaluation, as well as an extensive validation with wind tunnel data and high-fidelity Delayed Detached Eddy Simulations (DDES) using a wall-resolved mesh with $y^+ < 1$ [35].

The methodology has demonstrated to be effective across multiple aerodynamic studies on high-performance vehicles under diverse operating conditions [20,34,36,37], offering a good balance between computational efficiency and solution fidelity, well-suited for this research. This paper presents the essential details of this methodology with respect to the specification of the computational domain, meshing strategy, and solving method, with further details available in the referenced works.

The vehicle is simulated within a rectangular computational domain, illustrated in Figure 2, featuring a velocity-inlet 3 car-lengths (L) upstream and a pressure-outlet 5L downstream of the vehicle, following modelling guidelines for automotive aerodynamics [38]. Side and top walls, positioned 1.5L from the vehicle, are assigned with symmetry conditions to prevent boundary layer growth. Moving ground and wheel rotation velocities, listed along with other simulations settings in Table 2, match the free-stream velocity of 29 m/s, equivalent to a Reynolds number of 8.88×10^6. Turbulence conditions follow on-road measurements [39], ensuring representative operating conditions.

The overset mesh approach used in [20,34] is deployed to construct the computational domain with individual unstructured poly-hexcore meshes in ANSYS Fluent Meshing. This method interpolates data in overlapping mesh regions, enabling targeted transformations of aerodynamic device component meshes without needing to re-mesh the entire domain. Mesh settings include a base element and vehicle surface element size of approximately 7.25% and 0.45% of the vehicle's length, respectively. To improve resolution on aerodynamic devices and small geometric features, vehicle surface element sizes are locally reduced by over 80%. A medium near-wall treatment with a y^+ range of 120–150 and 4–6 inflation layers is applied, adhering to the recommended y^+ range by ANSYS Fluent

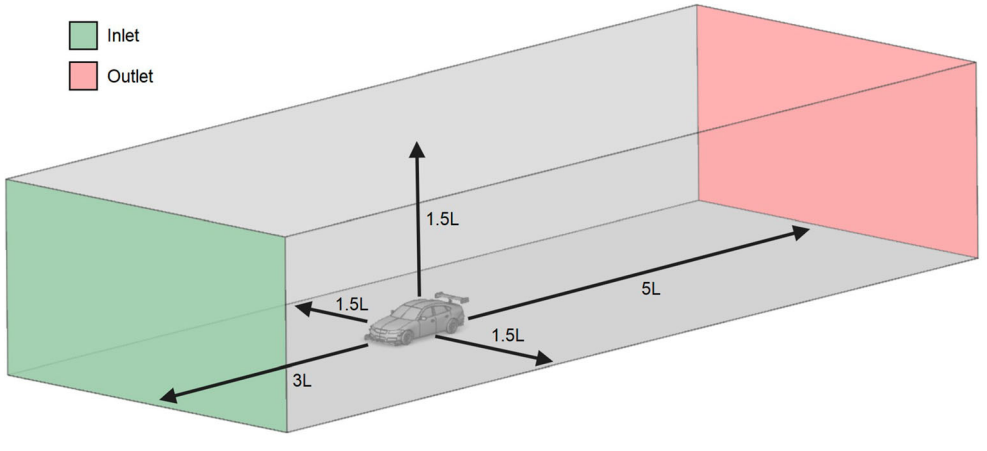

Figure 2. Illustration of the computational domain.

Table 2. Computation fluid dynamics simulation settings.

Setting	Value	Unit
Inlet & Outlet		
Velocity-inlet	29	m/s
Turbulent intensity	4	%
Turbulent length scale	2.5	m
Pressure-outlet	0	Pa
Moving walls		
Ground plane, *translational*	29	m/s
Wheels, *rotational*	91.3	rad/s
Air properties		
Density	1.204	kg/m^3
Dynamic viscosity	$1.813e^{-5}$	kg/(m s)
Temperature	293	K

[40] for the selected turbulence model. Additionally, refinement zones are incorporated to enhance resolution in the vehicle's near-field and wake regions. The resulting mesh, illustrated in Figure 3, contains approximately 23.9 million cells, with over 99% of the cells achieving an orthogonal quality greater than 0.7.

Simulations are conducted using the k-ω SST RANS turbulence model [41] in ANSYS Fluent, solving the continuity, momentum, and transport equations for turbulent kinetic energy and specific dissipation rate. Pressure-velocity coupling is performed with the coupled scheme, and spatial discretisation with the second-order upwind scheme. Convergence is assessed by monitoring the moving means of the lift, drag, and side force coefficients, which typically stabilised within 200 iterations. Additionally, residuals are tracked to ensure numerical stability, with continuity, turbulent kinetic energy, and specific dissipation rate residuals stabilising below $1e^{-2}$, and the x-, y-, and z-velocity residuals stabilising below $1e^{-6}$ within this iteration range. Each simulation is therefore performed for 750 iterations, with data averaged over the final 450 iterations. The simulations are conducted on two nodes consisting of AMD EPYC 7543 processors, utilising 128 cores, and averaging approximately 5 h per simulation.

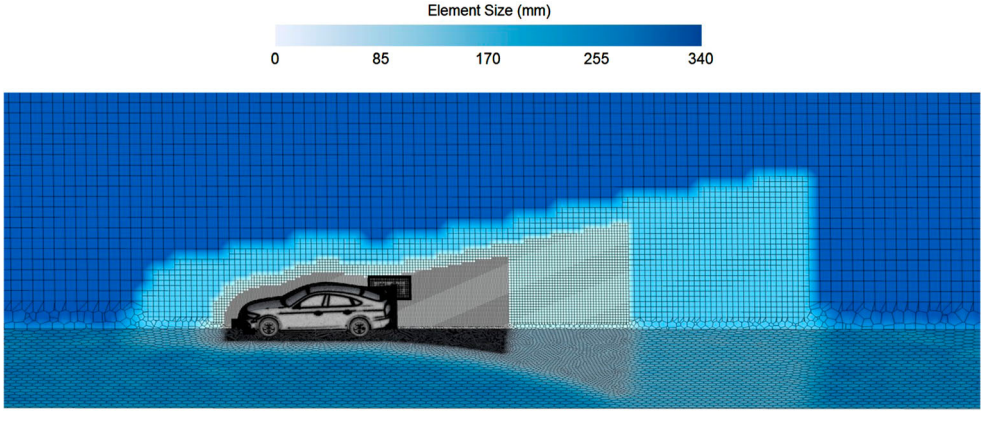

Figure 3. Element sizes near the vehicle visualised using a symmetry slice. Reproduced from Rijns et al. 'Performance analyses of active aerodynamic load balancing designs on high-performance vehicles in cornering conditions', Phys. Fluids, **36**(8), 085199 (2024a), with the permission of AIP Publishing.

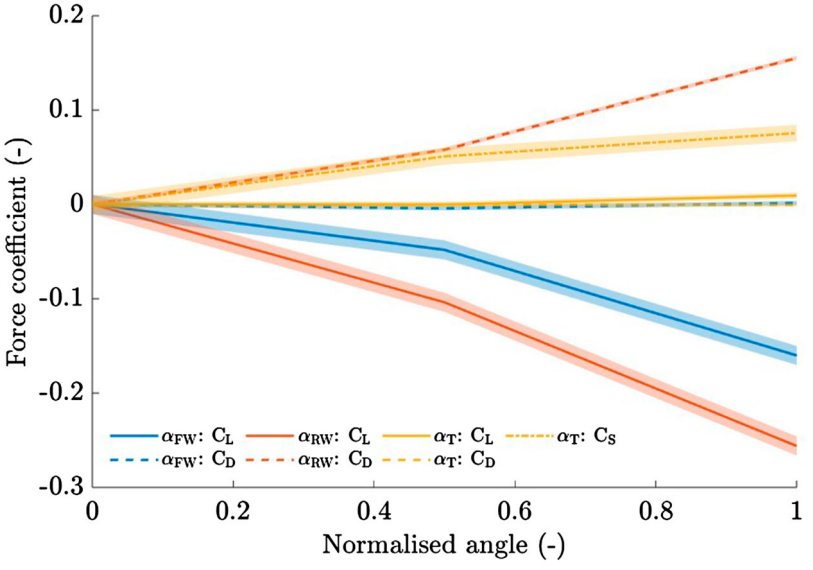

Figure 4. The effects of front wing angle, rear wing angle, and rear wing tilt on the vehicle's lift, drag, and side force coefficients. The shaded bars show mean average deviation, indicating parameter interdependence.

3.1. Aerodynamic systems interdependencies

Prior to running the full suite of simulations for all wing angle combinations, an initial interdependency analysis is conducted to determine if the front wing angle of attack α_{FW}, rear wing angle of attack α_{RW}, and rear wing tilt angle α_{TW} independently affect aerodynamic performance. The parameters are simulated at minimum, median, and maximum angles to create a combination space. Interdependencies are quantified by the mean average deviation (MAD) of combination sweeps relative to results obtained for a single parameter sweep with zero inputs for the other parameters.

The aerodynamic effects of each parameter are shown in Figure 4, with shaded bars representing the maximum MAD. MAD values for lift, drag, and side forces remain below 1.5%, 0.5%, and 10% of their respective maximum force coefficients, though similar in absolute terms. Treating the aerodynamic inputs as independent variables introduces an average absolute force coefficient uncertainty of 0.005, less than 1% of the vehicle's maximum force coefficient, while reducing the required simulations by over 97% from 1331 to 33 when sampled at finer one-tenth intervals of each parameter's maximum angle. This approach streamlines the computational process while preserving the essential aerodynamic effects, making it well-suited for the aims of this study.

4. Vehicle model

This study employs a seven degree of freedom planar vehicle model, illustrated in Figure 5, to simulate the impact of active aerodynamic systems on vehicle performance, building on established mathematical formulations [30,42]. The model incorporates both longitudinal and lateral load transfer, along with non-linear tyre characteristics, which are essential for

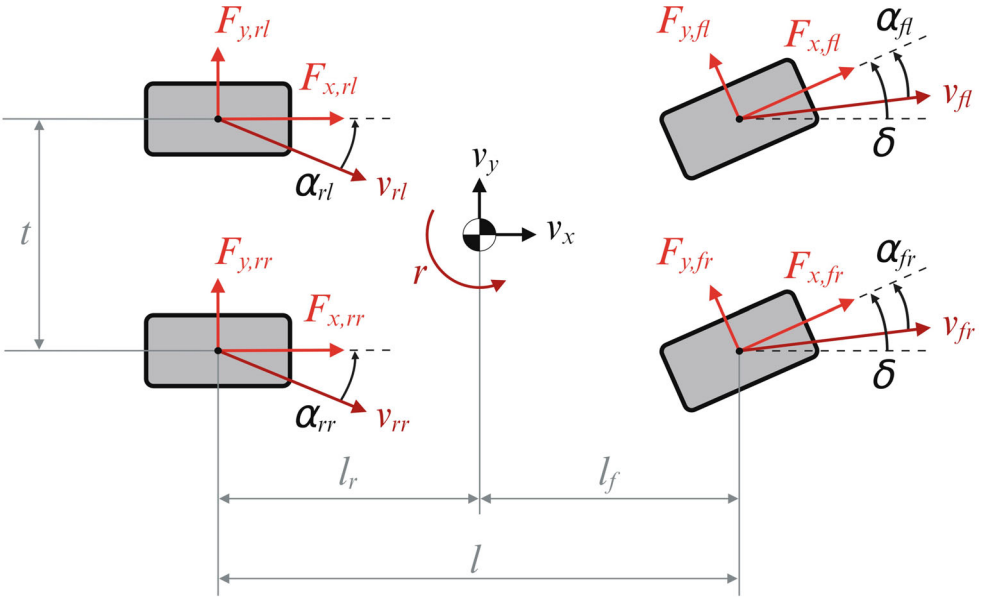

Figure 5. Vehicle dynamics model.

capturing the strong relation between aerodynamic loads and tyre force generation. Table 1 provides an overview of the fixed vehicle parameters, based on the vehicle's geometry and representative specifications for sports and racing vehicles from [43], which are used in the model.

Trajectory tracking is performed in a curvilinear coordinate system to align with the optimisation framework discussed in Section 5. The vehicle's position is expressed in terms of its travelled distance along the track's centre line s (m), the distance perpendicular to the track's centre line n (m), and the angle relative to the track's centre line tangent ϵ (rad), as expressed by Equations (1)–(3). Here, t (s) denotes time, κ (m^{-1}) the curvature of the track's centre line, v_x (m/s) the vehicle's longitudinal velocity, v_y (m/s) the vehicle's lateral velocity, and r (rad/s) the vehicle's yaw rate.

$$\frac{\mathrm{d}}{\mathrm{d}t}s = \frac{v_x \cos(\epsilon) - v_y \sin(\epsilon)}{1 - n\kappa} \tag{1}$$

$$\frac{\mathrm{d}}{\mathrm{d}t}n = v_x \sin(\epsilon) + v_y \cos(\epsilon) \tag{2}$$

$$\frac{\mathrm{d}}{\mathrm{d}t}\epsilon = r - \kappa \frac{\mathrm{d}}{\mathrm{d}t}s \tag{3}$$

Section 5 motivates the use of travelled distance as the independent variable in the optimisation simulations, replacing time to reduce computational complexity and enhance efficiency. Following the methodology in [21], time-dependent equations are transformed into distance-dependent formulations by introducing the scaling factor S_f, which represents the inverse of Equation (1) ($\mathrm{d}t/\mathrm{d}s$). This transformation, applied in Equations (4)

and (5), ensures that the equations remain consistent within the distance-based optimisation framework.

$$\frac{\mathrm{d}}{\mathrm{d}s}n = \Big(v_x \sin(\epsilon) + v_y \cos(\epsilon)\Big)\, S_f \tag{4}$$

$$\frac{\mathrm{d}}{\mathrm{d}s}\epsilon = S_f\, r - \kappa \tag{5}$$

The vehicle's equations of motion, expressed as a function of travelled distance, are described by Equations (6)–(8). Throughout these equations, subscripts are used to denote specific components, where k represents the longitudinal (x), lateral (y), or vertical (z) direction, i specifies the front (f) or rear (r) axle location, and j indicates the left (l) or right (r) wheel position.

In these equations, $F_{k,ij}$ (N) denotes the tyre forces, δ (rad) the steering angle, m (kg) the vehicle's total mass, F_R (N) the rolling resistance force, and I_z (kg m^2) the yaw moment of inertia. The parameter l_i (m) defines the distance from each axle to the centre of gravity (COG) and t_w (m) the vehicle's track width. Additionally, F_D (N) represents the total aerodynamic drag force opposing the vehicle's motion, while F_S (N) and $F_{S,i}$ (N) correspond to the total aerodynamic side force and its components acting on the front and rear axles, respectively, with their positive direction matching that of the lateral tyre forces.

$$\begin{aligned}\frac{\mathrm{d}}{\mathrm{d}s}v_x = \Big[&(F_{x,fl} + F_{x,fr})\cos(\delta) - (F_{y,fl} + F_{y,fr})\sin(\delta) \\ &+ F_{x,rl} + F_{x,rr} + m\, v_y\, r - F_D - F_R\Big]\frac{S_f}{m}\end{aligned} \tag{6}$$

$$\begin{aligned}\frac{\mathrm{d}}{\mathrm{d}s}v_y = \Big[&(F_{y,fl} + F_{y,fr})\cos(\delta) + (F_{x,fl} + F_{x,fr})\sin(\delta) \\ &+ F_{y,rl} + F_{y,rr} - m\, v_x\, r + F_S\Big]\frac{S_f}{m}\end{aligned} \tag{7}$$

$$\begin{aligned}\frac{\mathrm{d}}{\mathrm{d}s}r = \Bigg[&\Big((F_{x,fl} + F_{x,fr})\sin(\delta) + (F_{y,fl} + F_{y,fr})\cos(\delta) + F_{S,f}\Big)\, l_f \\ &- \Big(F_{y,rl} + F_{y,rr} + F_{S,r}\Big)\, l_r + \Big(F_{x,rr} - F_{x,rl}\Big)\,\frac{t_w}{2} \\ &+ \Big((F_{x,fr} - F_{x,fl})\cos(\delta) + (F_{y,fl} - F_{y,fr})\sin(\delta)\Big)\,\frac{t_w}{2}\Bigg]\frac{S_f}{I_z}\end{aligned} \tag{8}$$

Wheel dynamics are expressed by Equation (9), where Ω_{ij} (rad/s) represents the wheel's angular velocity, T_{ij} (Nm) the applied wheel torque, R_w (m) the wheel radius, and I_w (kg m^2) the wheel's rotational inertia.

$$\frac{\mathrm{d}}{\mathrm{d}s}\Omega_{ij} = \Big(T_{ij} - F_{x,ij}\, R_w\Big)\,\frac{S_f}{I_w} \tag{9}$$

4.1. Tyres

The longitudinal and lateral tyre forces are dependent on the vertical forces acting on the tyres. These vertical loads are described by Equation (10), where the first term represents

the static weight distribution, with g (m^2/s) denoting the gravitational acceleration, $m_{u,i}$ (kg) the unsprung masses, m_s (kg) the sprung mass, and l (m) the wheelbase length. Additionally, $F_{L,ij}$ (N) indicates the aerodynamic lift force acting on each individual wheel, and $\Gamma_{x,ij}$ (N) and $\Gamma_{y,ij}$ (N) denote the components of longitudinal and lateral load transfer experienced by each individual wheel.

$$F_{z,ij} = \frac{1}{2} g \left(m_{u,i} + m_s \frac{l_i}{l} \right) - F_{L,ij} \pm \Gamma_{x,ij} \pm \Gamma_{y,ij} \tag{10}$$

The longitudinal and lateral tyre forces are modelled using the Pacejka '96 model [44], as expressed by Equations (11) and (12). The Pacejka coefficients, derived from 250/570R13 Avon British F3 tyre data at 0° camber [45], are detailed in Table 3.

$$F_{x,ij} = D_{x,ij} \sin \left[C_x \tan^{-1} \left\{ B_x s_{ij} - E_x \left(B_x s_{ij} - \tan^{-1}(B_x s_{ij}) \right) \right\} \right] \tag{11}$$

$$F_{y,ij} = D_{y,ij} \sin \left[C_y \tan^{-1} \left\{ B_y \alpha_{ij} - E_y \left(B_y \alpha_{ij} - \tan^{-1}(B_y \alpha_{ij}) \right) \right\} \right] \tag{12}$$

The peak value $D_{k,ij}$ (-) is dependent on the tyre's friction coefficient μ_{ij} (-), which are both load dependent as described by Equations (13) and (14). Here, μ_0 (-) denotes the tyre's coefficient of friction at the nominal vertical wheel load F_{z0} (N), and P_{D2} (-) represents the Pacejka coefficient for variation of friction with load.

$$D_{k,ij} = \mu_{ij} F_{z,ij} \tag{13}$$

$$\mu_{k,ij} = \mu_0 + P_{D2} \frac{F_{z,ij} - F_{z0}}{F_{z0}} \tag{14}$$

The longitudinal and lateral forces produced by each tyre are dependent on the slip ratio s_{ij} (-) and slip angle α_{ij} (rad), described by Equations (15)–(17). Here, v_{ij} (m/s) denotes the effective velocity of the tyre and is expressed by Equation (18).

$$\alpha_{fj} = \delta - \tan^{-1} \left(\frac{r\, l_f + v_y}{v_x \pm r \frac{t_w}{2}} \right) \tag{15}$$

$$\alpha_{rj} = \tan^{-1} \left(\frac{r\, l_r - v_y}{v_x \pm r \frac{t_w}{2}} \right) \tag{16}$$

Table 3. Tyre model coefficients.

Coefficient	Value	Description
F_{z0}	4905	Nominal Load (N)
μ_0	1.41	Friction coefficient
P_{D2}	−0.6	Variation of friction with load
B_x	6	Stiffness factor, longitudinal
C_x	2.3	Shape factor, longitudinal
E_x	0.9	Curvature factor, longitudinal
B_y	6	Stiffness factor, lateral
C_y	2.5	Shape factor, lateral
E_y	0.5	Curvature factor, lateral

$$s_{ij} = \frac{R_w \, \Omega_{ij} - v_{ij}}{v_{ij}} \tag{17}$$

$$v_{ij} = \cos(\alpha_{ij}) \sqrt{\left(v_y \pm r \, l_i\right)^2 + \left(v_x \pm r \, \frac{t_w}{2}\right)^2} \tag{18}$$

Finally, the rolling resistance is modelled using a constant friction coefficient C_f (-) and the vehicle's total vertical load, as expressed by Equation (19), incorporating aerodynamic load effects on rolling resistance.

$$F_R = C_f \left(F_{z,fl} + F_{z,fr} + F_{z,rl} + F_{z,rr}\right) \tag{19}$$

4.2. Load transfer

Longitudinal and lateral load transfer occur due to inertial forces which resist the traction forces produced by the tyres. These inertial forces act at the centre of gravity height h_{COG} (m), creating an overturning moment that causes load transfer. The total longitudinal load transfer Γ_x (N) is described by Equation (20), where the nominal drag force F_D^0 (N), which represents the vehicle's drag without any aerodynamic device actuation, is also assumed to act at the centre of gravity height. Section 6.1 will discuss that additional drag generated by the aerodynamic systems F_D^{aero} (N) is primarily produced by the rear wing, and is therefore assumed to act at the rear wing height h_{RW} (m). The longitudinal load transfer experienced by each individual wheel is equal to half of the total longitudinal load transfer.

$$\begin{aligned} \Gamma_x = \big[&(F_{x,fl} + F_{x,fr}) \cos(\delta) - (F_{y,fl} + F_{y,fr}) \sin(\delta) \\ &+ F_{x,rl} + F_{x,rr} + F_D^0\big] \frac{h_{COG}}{l} + F_D^{\text{aero}} \frac{h_{RW}}{l} \end{aligned} \tag{20}$$

The total lateral load transfer Γ_y (N) is expressed by Equation (21). Similar to drag, aerodynamic side force F_S (N) is predominantly generated by the rear wing and is therefore assumed to act at the rear wing height.

$$\begin{aligned} \Gamma_y = \big[&(F_{x,fl} + F_{x,fr}) \sin(\delta) + (F_{y,fl} + F_{y,fr}) \cos(\delta) \\ &+ F_{y,rl} + F_{y,rr}\big] \frac{h_{COG}}{t_w} + F_S \frac{h_{RW}}{t_w} \end{aligned} \tag{21}$$

The distribution of lateral load transfer across the front and rear axles is expressed by Equations (22)–(24), where $C_{\Gamma y,i}$ (-) denotes the axle-specific fraction of total lateral load transfer. The equations consider contributions from the unsprung masses, the sprung mass via the suspension links, and the roll couple of the sprung mass through the springs. It depends on vehicle parameters such as unsprung mass heights $h_{u,i}$ (m), roll centre heights h_i (m), and the distance between the COG and the roll axis d (m). While most parameters have limited modifiability due to inherent design constraints, the roll stiffness distribution γ_{k_ϕ} (-), which defines the fraction of total roll stiffness k_ϕ (Nm/rad) at the rear axle, offers

some tunability.

$$\Gamma_{y,ij} = \frac{C_{\Gamma y,i}}{C_{\Gamma y,f} + C_{\Gamma y,r}} \Gamma_y \tag{22}$$

$$C_{\Gamma y,f} = \frac{h_{u,f}\, m_{u,f}}{t_w\, m} + \frac{l_r\, h_f\, m_s}{l\, t_w\, m} + \frac{(1-\gamma_{k_\phi})\, k_\phi\, m_s \left(\frac{d}{k_\phi - m_s\, g\, d}\right)}{t_w\, m} \tag{23}$$

$$C_{\Gamma y,r} = \frac{h_{u,r}\, m_{u,r}}{t_w\, m} + \frac{l_f\, h_r\, m_s}{l\, t_w\, m} + \frac{\gamma_{k_\phi}\, k_\phi\, m_s \left(\frac{d}{k_\phi - m_s\, g\, d}\right)}{t_w\, m} \tag{24}$$

4.3. Aerodynamics

The aerodynamic performance of the vehicle equipped with active aerodynamic systems is obtained from CFD simulations, as described in Section 3, and incorporated into the optimisation framework using polynomial functions. These functions describe the influence of each aerodynamic control input on both the magnitude and distribution of aerodynamic loads acting on the vehicle. Specifically, the effects on key aerodynamic force components, including lift at the front $C_{L,\text{front}}$ (-) and rear wheels $C_{L,\text{rear}}$ (-), lift at the left $C_{L,\text{left}}$ (-) and right wheels $C_{L,\text{right}}$ (-), side force at the front $C_{S,\text{front}}$ (-) and rear axles $C_{S,\text{rear}}$ (-), and total drag C_D (-), are expressed using polynomial formulations.

Rather than explicitly modelling aerodynamic moments about a fixed reference point, the resulting force distributions are applied directly at the four wheels. This approach not only captures the effects of both net forces and resulting moments through the relative positioning of the loads, but is also more convenient in the context of active aerodynamics, where the effective point of action of aerodynamic forces can vary with system actuation. In this way, aerodynamic lift, drag, and side forces are consistently translated into changes in vertical load at each tyre, which in turn form the basis for calculating longitudinal and lateral forces at the tyre–road interface.

Equation (25) provides a general formulation for the effect of an aerodynamic element on a given force component coefficient $\Delta C^w_{u,v}$ (-), as a function of its operating angle α_w (deg). The aerodynamic elements are indexed by $w \in \{\text{FW}-\text{L}, \text{FW}-\text{R}, \text{RW}, \text{TW}\}$, corresponding to the left front wing angle, right front wing angle, rear wing angle, and rear wing tilt. The aerodynamic lift, drag, and side forces are represented by $u \in \{L, D, S\}$, while $v \in \{\text{front}, \text{rear}, \text{left}, \text{right}\}$ specifies the force distribution location. The polynomial coefficients $P^w_{u,v}(\ell)$ (-) define the aerodynamic response, ℓ (-) indexes the polynomial terms, and $N^w_{u,v}$ (-) denotes the polynomial order. The polynomial coefficients for each aerodynamic element's influence on the respective force components are detailed in Table 4.

$$\Delta C^w_{u,v} = \sum_{\ell=1}^{N^w_{u,v}} P^w_{u,v}(\ell)\, \alpha_w^{\ell} \tag{25}$$

The combined aerodynamic force component coefficients $C_{u,v}$ (-) are successively obtained by summing the individual effects from all active aerodynamic elements with the vehicle's nominal coefficients $C^0_{u,v}$ (-), which represent the aerodynamic characteristics without any system actuation, as described in Equation (26). The total aerodynamic force coefficients are subsequently determined by summing the relevant component contributions, as

Table 4. Coefficients for the aerodynamic relationships.

Coefficient	$C_{L,front}$	$C_{L,rear}$	$C_{L,left}$	$C_{L,right}$	C_D	$C_{S,front}$	$C_{S,rear}$
$C^0_{u,v}$	−0.188	−0.103	−0.146	−0.146	0.346	0	0
$P^{FR-L}_{u,v}(1)$	$-9.75e^{-3}$	$1.58e^{-3}$	$-8.17e^{-3}$	0	0	0	0
$P^{FR-R}_{u,v}(1)$	$-9.75e^{-3}$	$1.58e^{-3}$	0	$-8.17e^{-3}$	0	0	0
$P^{RW}_{u,v}(1)$	$3.79e^{-3}$	$-2.18e^{-2}$	$-9.01e^{-3}$	$-9.01e^{-3}$	$2.90e^{-3}$	0	0
$P^{RW}_{u,v}(2)$	$-1.94e^{-4}$	$1.11e^{-3}$	$4.32e^{-4}$	$4.32e^{-4}$	$7.87e^{-5}$	0	0
$P^{RW}_{u,v}(3)$	$4.31e^{-6}$	$1.56e^{-5}$	$9.95e^{-6}$	$9.95e^{-6}$	0	0	0
$P^{RW}_{u,v}(4)$	0	$-2.75e^{-6}$	$-1.37e^{-6}$	$-1.37e^{-6}$	0	0	0
$P^{RW}_{u,v}(5)$	0	$4.92e^{-8}$	$2.46e^{-8}$	$2.46e^{-8}$	0	0	0
$P^{TW}_{u,v}(1)$	0	$-7.1e^{-5}$	$4.30e^{-3}$	$-4.30e^{-3}$	0	0	$7.19e^{-3}$
$P^{TW}_{u,v}(2)$	0	0	$3.55e^{-5}$	$3.55e^{-5}$	0	0	0

exemplified for lift in Equation (27).

$$C_{u,v} = C^0_{u,v} + \Delta C^{FW-L}_{u,v} + \Delta C^{FW-R}_{u,v} + \Delta C^{RW}_{u,v} + \Delta C^{TW}_{u,v} \tag{26}$$

$$C_L = C_{L,front} + C_{L,rear} \tag{27}$$

Given the critical role of aerodynamic loads in tyre force generation, lift coefficients are formulated for each wheel to enable direct integration with the vertical tyre load formulation in the vehicle dynamics model. The distribution is determined based on the side-specific lift contributions previously established. Equation (28) describes this process for the front left wheel, with analogous expressions for the front right, rear left, and rear right wheels.

$$C_{L,FL} = C_{L,front} \frac{C_{L,left}}{C_L} \tag{28}$$

Finally, the aerodynamic forces $F_{u,v}$ (N) acting on the vehicle are computed using Equation (29), where ρ (kg/m^3) is the air density, A_{ref} (m^2) the vehicle's reference frontal area, and v_x (m/s) the longitudinal velocity.

$$F_{u,v} = \frac{1}{2} \rho \, C_{u,v} \, A_{ref} \, {v_x}^2 \tag{29}$$

4.4. Powertrain

The powertrain is modelled as an electric motor unit coupled with a single-speed transmission and a central differential, enabling torque distribution between the front and rear axles for four-wheel drive capability. Performance metrics are derived from an existing motorsport electric propulsion system [46], with a maximum continuous power output $P_{e,max}$ of 456 kW, a maximum continuous torque output $T_{e,max}$ of 602 Nm, and a maximum motor speed $\Omega_{e,max}$ of 17750 RPM. The electric motor torque T_e (Nm) is used to determine the individual wheel torques, as expressed by Equations (30) and (31). Here, γ_T (-) denotes the fixed torque distribution, defining the fraction of total torque directed to the rear axle, and γ_g (-) represents the final gear ratio. Additionally, T_b (Nm) represents the braking torque averaged over all wheels, and γ_b (-) the fixed brake balance, defining the fraction of total

braking torque directed to the front wheels.

$$T_{fj} = \frac{1}{2}\left((1-\gamma_T)\,T_e\,\gamma_g + T_b\,\gamma_b\right) \tag{30}$$

$$T_{rj} = \frac{1}{2}\left(\gamma_T\,T_e\,\gamma_g + T_b\,(1-\gamma_b)\right) \tag{31}$$

5. Optimisation framework

This study utilises an optimisation framework developed by Jiménez et al. [30], which aims to minimise lap time by optimising the vehicle's trajectory, control inputs, and parameter combinations while adhering to track constraints and vehicle performance limitations. This Minimum Lap Time Problem (MLTP) is formulated as an Optimal Control Problem (OCP) and transformed into a Non-Linear Program (NLP) using direct orthogonal collocation. A brief overview is provided here, with a more comprehensive explanation available in the work by Jiménez et al. [30].

5.1. Optimal control problem

The OCP is formulated to optimise the vehicle states $\boldsymbol{x}$, control inputs $\boldsymbol{u}$, auxiliary variables $\boldsymbol{y}$ and selected vehicle design parameters $\boldsymbol{p}$ to minimise total lap time. The distance travelled along the track is used as the independent variable, a method successfully applied in prior studies [21,28,42], which maintains an explicit connection to the track position and reduces computational complexity by lowering the problem's dimensionality.

The objective function, expressed by Equation (32), is constrained by Equations (33)–(35), with the optimisation variables specified in Equation (36). The start and finish positions are denoted by s_0 and s_f. The vector function $\boldsymbol{f}$ describes the vehicle's dynamics through Equations (4)–(9), which are enforced as constraints to ensure accurate simulation of the vehicle's performance. The vector function $\boldsymbol{h}$ defines constraints on the optimisation variables through bounds and additional constraints defined by Equations (37)–(42). Initial and final states are described by $\boldsymbol{b}$, used to define the vehicle's starting and finishing conditions.

Minimise

$$J = \int_{s_0}^{s_f} S_f\left(\boldsymbol{x}(s), \boldsymbol{u}(s), \boldsymbol{y}(s), \boldsymbol{p}\right) \mathrm{d}s \tag{32}$$

Subject to

$$\frac{\mathrm{d}}{\mathrm{d}s}\boldsymbol{x} = \boldsymbol{f}\left(\boldsymbol{x}(s), \boldsymbol{u}(s), \boldsymbol{y}(s), \boldsymbol{p}\right) \tag{33}$$

$$\boldsymbol{h}\left(\boldsymbol{x}(s), \boldsymbol{u}(s), \boldsymbol{y}(s), \boldsymbol{p}\right) \leq 0 \tag{34}$$

$$\boldsymbol{b}\left(\boldsymbol{x}(s_0), \boldsymbol{x}(s_f)\right) = 0 \tag{35}$$

With

$$\boldsymbol{x} = \begin{bmatrix} v_x \\ v_y \\ r \\ n \\ \eta \\ \Omega_{ij} \end{bmatrix}, \quad \boldsymbol{u} = \begin{bmatrix} T_e \\ T_b \\ \delta \\ \alpha_{FW(-j)} \\ \alpha_{RW} \\ \alpha_{TW} \end{bmatrix}, \quad \boldsymbol{y} = \begin{bmatrix} \Gamma_x \\ \Gamma_y \end{bmatrix}, \quad \text{and} \quad \boldsymbol{p} = \begin{bmatrix} \gamma_b \\ \gamma_T \\ \gamma_{k_\phi} \end{bmatrix} \tag{36}$$

Limitations on the maximum electric motor power and angular velocity are incorporated through Equations (37) and (38), while Equation (39) prevents simultaneous application of drive and brake torque control inputs, avoiding unrealistic driving scenarios. Tyre grip is constrained by a friction circle model with a uniform friction coefficient in both longitudinal and lateral directions, as expressed by Equation (40), ensuring tyre forces remain within the available grip. Finally, longitudinal and lateral load transfer are incorporated as auxiliary variables through equality constraints given by Equations (41) and (42).

$$\Omega_e \, T_e - P_{e,\max} \leq 0 \tag{37}$$

$$\Omega_e - \Omega_{e,\max} \leq 0 \tag{38}$$

$$T_e \, T_b = 0 \tag{39}$$

$$\frac{{F_{x,ij}}^2 + {F_{y,ij}}^2}{{F_{z,ij}}^2} - {\mu_{ij}}^2 \leq 0 \tag{40}$$

$$\Gamma_x - \Bigg[\big((F_{x,fl} + F_{x,fr}) \cos(\delta) - (F_{y,fl} + F_{y,fr}) \sin(\delta) + F_{x,rl} + F_{x,rr} + F_D^0\big) \frac{h_{COG}}{l} + F_D^{\text{aero}} \frac{h_{RW}}{l} \Bigg] = 0 \tag{41}$$

$$\Gamma_y - \Bigg[\big((F_{x,fl} + F_{x,fr}) \sin(\delta) + (F_{y,fl} + F_{y,fr}) \cos(\delta) + F_{y,rl} + F_{y,rr}\big) \frac{h_{COG}}{t_w} + F_S \frac{h_{RW}}{t_w} \Bigg] = 0 \tag{42}$$

5.2. Non-Linear programming

The continuous-time OCP is discretised and transcribed into a NLP problem using direct orthogonal collocation to enable numerical optimisation. This involves dividing the track into N segments, each of length ds_k (m). Within each segment s_k, the states are approximated using Legendre polynomials of degree d, where collocation points $s_{k,j}$, with $j = \{1, \ldots, d\}$, are selected at the roots of these polynomials. Collocation constraints are enforced at each collocation point, matching the polynomial derivatives of the approximated states to equations governing the vehicle's dynamics. This ensures that the approximated vehicle trajectory evolves according to its modelled dynamic behaviour.

The objective function is evaluated at the collocation points within each track segment, defined by the vector function $\boldsymbol{S}_{f,k} = [S_f(s_{k,1}), \ldots, S_f(s_{k,d})]$. The contribution of each track segment is weighted by $\boldsymbol{B}$, ensuring that the integral of the objective function over the entire track is accurately approximated. These weighted contributions are summed across

all track segments to provide the NLP formulation of the objective function, as expressed by the first term in Equation (43).

$$J = \sum_{k=1}^{N} \boldsymbol{BS}_{f,k}\, \mathrm{d}s_k + \underbrace{\sum \left(r_m \Delta_s^m U_k\right)^2 + \sum \left(r_m \Delta_s^m Y_k\right)^2}_{\text{regularisation}} \tag{43}$$

To ensure realistic and feasible solutions, additional constraints and regularisation terms are introduced. Physical limitations of control inputs are enforced through rate limits, preventing unrealistic steering inputs and reflecting system response times. Regularisation terms are incorporated in the objective function to promote more practical solutions by penalising the sum of squares of specific discrete control inputs U_k, auxiliary variables Y_k, and their m-th derivatives at each track segment Δ_s^m. The regularisation weight factors r_m allow adjustment of each term's influence in the optimisation process.

5.3. Setup

The vehicle performance optimisation simulations are performed on the Circuit de Barcelona-Catalunya, a track known for its combination of high-speed straights and technical corners, making it ideal for comprehensive vehicle performance evaluations. As the track serves solely as a representative case encompassing diverse driving scenarios for the comparative assessment of different aerodynamic configurations, track-specific features such as elevation changes are not included.

The NLP problem is solved using the IPOPT algorithm in MATLAB, with an optimality tolerance of 1×10^{-6} and constraint violation tolerances of 1×10^{-4}. Based on grid convergence data presented in Figure 6, a discretisation step size of 10 m is selected, achieving a relative lap time error of approximately 0.01% compared to the smallest step size tested, while reducing computational time by over 23%. Following the work of Jiménez et al.

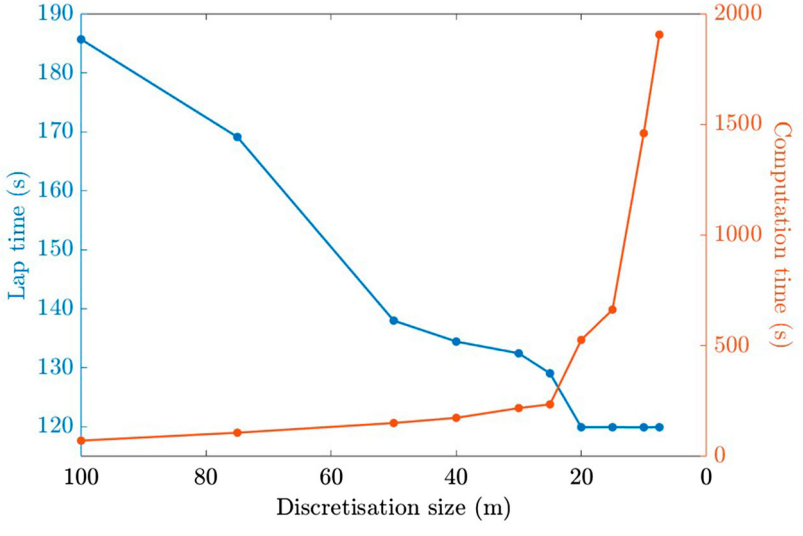

Figure 6. Lap time and computation time as a function of the discretisation step size.

Table 5. Rate limits and regularisation weight factors for control inputs and auxiliary variables used for the performance optimisation simulations.

Parameter	Symbol	Rate limits		Regularisation		
		Lower	Upper	r_0	r_1	r_2
Drive torque	T_e	$-2e^4$ Nm/s	$2e^4$ Nm/s	0	0	0
Brake torque	T_b	$-2e^4$ Nm/s	$2e^4$ Nm/s	0	0	0
Steering angle	δ	−0.1 rad/s	0.1 rad/s	0	10	15
Front wing angle	α_{FW}	−20 deg/s	20 deg/s	0	0	0.3
Rear wing angle	α_{RW}	−60 deg/s	60 deg/s	0	0	0.9
Rear wing tilt	α_{TW}	−24 deg/s	24 deg/s	0.005	0	0.4
Longitudinal load transfer	Γ_x	–	–	0	0	1

[30], 3rd order Legendre polynomials are used to approximate the states within each track segment.

Control input rate limits and regularisation weight factors used to ensure practical solutions are detailed in Table 5. The rate limits reflect system and driver response times, with aerodynamic systems specifically constrained based on reported response times of approximately 0.5 s in existing high-performance active aerodynamic systems. Furthermore, the regularisation factors are carefully tuned to suppress high-frequency oscillations in the control inputs, ensuring smoother actuation. This prevents excessive corrections and allows clearer trends in the control strategies, supporting the consistency and interpretability of the findings in this study.

6. Results & discussions

The analyses begin with an examination of the impact of each aerodynamic element to understand how each component influences the vehicle's overall aerodynamic performance. Following this, the general performance of each configuration is analysed using lap time data, and areas of performance gains are identified using more detailed performance data. The subsequent section provides an in-depth analysis of the optimal control strategies for each aerodynamic system, offering insights into how these elements are controlled to realise the observed performance improvements. Finally, changes in some optimised key vehicle design parameters are assessed to explore how these parameters shift in response to different aerodynamic configurations.

6.1. Aerodynamic performance

The simulated aerodynamic data, which represent the effects of each aerodynamic element, along with the associated fitted functions used for implementation into the optimisation framework, are presented in Figure 7. The left and right front wing elements individually enhance front axle downforce by a maximum of approximately $\Delta C_L \approx -0.10$ across their respective angle of attack ranges, and affect the downforce on their respective sides of the vehicle by over $\Delta C_L \approx -0.08$. Each element also creates a minor reduction in rear axle downforce, up to approximately $\Delta C_L \approx 0.02$. Furthermore, the front wing elements have negligible effects on drag and downforce on their respective opposite side of the vehicle.

The rear wing exerts the most significant influence on aerodynamic performance. Across its angle of attack range, it increases rear axle downforce by an approximate

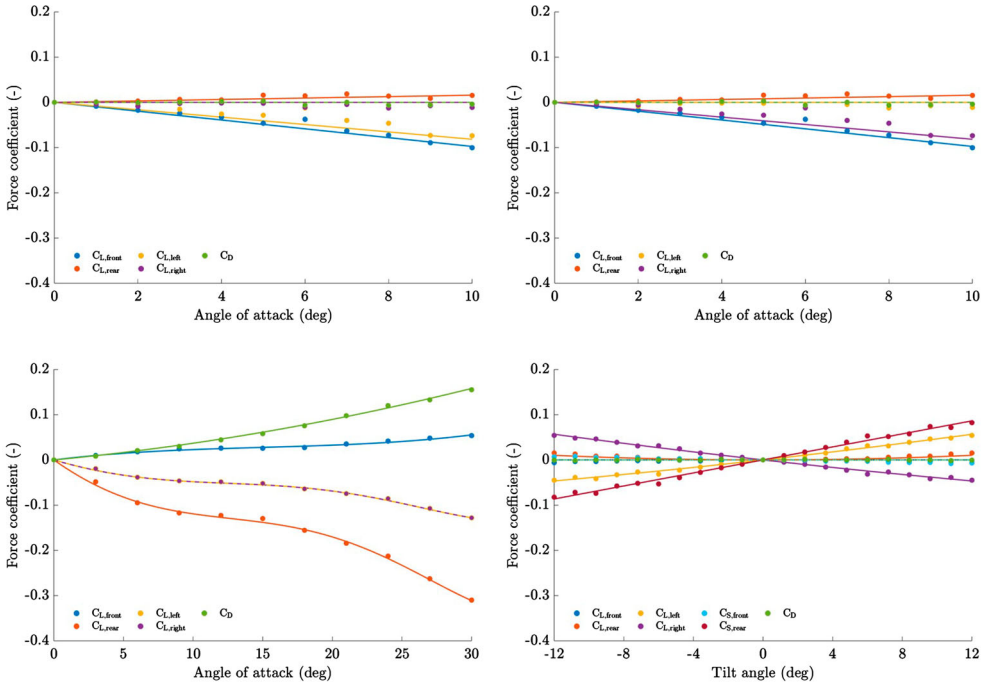

Figure 7. Simulated aerodynamic data and associated fitted functions for the effects of the (a) left front wing element angle of attack, (b) right front wing element angle of attack, (c) rear wing angle of attack, and (d) rear wing tilt angle on the vehicle's aerodynamic performance.

maximum of $\Delta C_L \approx -0.31$ but also reduces front axle downforce by over $\Delta C_L \approx 0.05$. The rear wing's symmetric configuration results in equal downforce distribution across the left and right sides of the vehicle. Notably, the rear wing exhibits two downforce gain regions, where initial enhancements plateau at the stall angle between 10°–15°, then rise further due to upstream pressurisation at higher angles, aligning with prior experimental findings [34]. Additionally, the rear wing increases drag by nearly $\Delta C_D \approx 0.16$ across its angle of attack range, with drag exhibiting a slight quadratic increase.

The rear wing tilt angle provides an additional layer of control by redistributing downforce laterally. Elevating one side of the wing increases downforce on that side by nearly $\Delta C_L \approx -0.05$, while decreasing it by almost $\Delta C_L \approx 0.06$ on the opposite side, resulting in a slight overall downforce reduction. The tilted rear wing also generates a side force primarily acting at the rear of the vehicle, directed toward the elevated side, and peaking at nearly $\Delta C_S \approx \pm 0.09$. Additionally, the tilt angle has minimal impact on front axle downforce and overall vehicle drag.

Building on the analysis of the individual effects of each aerodynamic element, the focus now shifts to assessing the vehicle's overall aerodynamic performance. The combined aerodynamic impact of symmetric front wing and rear wing angle of attack actuation, as presented in Figure 8, provides insight into the baseline aerodynamic characteristics of the vehicle. For improved visibility, the downforce coefficient is used in this figure instead of the lift coefficient.

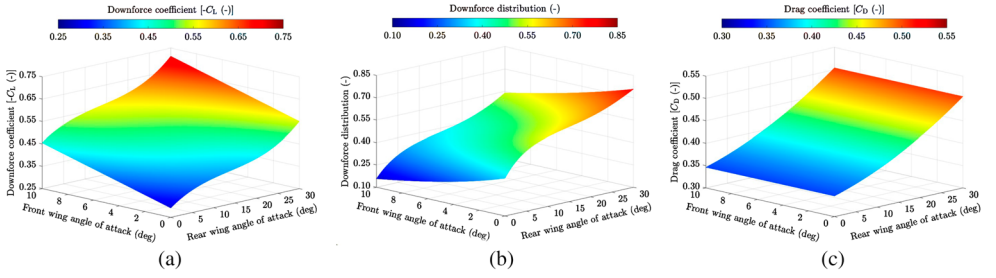

Figure 8. The impact of symmetric front and rear wing actuation on the vehicle's (a) downforce coefficient, (b) downforce distribution, representing the rear axle load fraction, and (c) drag coefficient.

At minimum front and rear wing angles of attack, the vehicle produces a baseline lift coefficient of $C_L \approx -0.29$ and a drag coefficient of $C_D \approx 0.35$. As the angles of attack increase, the rear wing's previously observed two-stage downforce enhancement regions become apparent, while the front wing contributes more linearly to the total downforce. Across their operating ranges, the rear wing increases the base downforce level $\Delta C_L \approx -0.26$ (+89%), and the front wing by $\Delta C_L \approx -0.16$ (+56%). Together, the wings enhance downforce by a total of $\Delta C_L \approx -0.42$ (+145%) to reach the maximum lift coefficient of $C_L \approx -0.71$.

The downforce distribution, representing the fraction of downforce on the rear axle, starts at approximately 0.35 at the minimum wing angles, indicating a forward bias. Maximising the rear wing angle while minimising the front wing angle shifts the distribution rearward to about 0.76. Conversely, minimising the rear wing angle and maximising the front wing angle shifts the distribution forward to approximately 0.16. With both wing angles maximised, the distribution balances around 0.54, showing a moderate rearward bias as the rear wing generates slightly more downforce at high angles of attack. Additionally, drag is primarily influenced by the rear wing, which increases the baseline drag level by $\Delta C_D \approx 0.16$ (+46%) to a maximum of $C_L \approx 0.50$ across its angle of attack range.

6.2. Vehicle performance

The analysis of lap times reveals clear performance distinctions between the four vehicle configurations, as detailed in Table 6. Configuration 1, with an optimised static setup using a maximum front wing angle of 10 degrees and a moderately low rear wing angle of around 8.12 degrees, records the longest lap time of 120.196 s, which serves as the baseline for comparison. Configuration 2, which operates with an optimised fixed front wing angle of 10 degrees and active rear wing control, achieves a lap time of 119.502 s, resulting in an improvement of 0.694 s (0.58% faster). Configuration 3, with active symmetric control over both the front and rear wings, records a lap time of 119.452 s, showing an improvement of 0.744 s (0.62% faster) over configuration 1. Finally, configuration 4, which has active asymmetric control of both front and rear wings, achieves the fastest lap time of 119.281 s, reducing lap time by 0.915 s (0.76% faster) compared to configuration 1.

The optimal racing line for configuration 1, shown in Figure 9, demonstrates the variety of driving scenarios encountered on a lap around the Circuit de Barcelona-Catalunya. Evidently, the ability of the active aerodynamic configurations to adapt to these driving

Table 6. Lap time results and optimised aerodynamic settings for all vehicle configurations.

Configuration	Front wing (deg)	Rear wing (deg)	Sector 1 time (s)	Sector 2 time (s)	Sector 3 time (s)	Lap time (s)	Δ Lap time (s)	Δ Lap time (%)
C1	10.000	8.121	32.953	45.085	42.158	120.196	–	–
C2	10.000	Active	32.721	44.795	41.986	119.502	0.694	0.58
C3	Active	Active	32.701	44.772	41.979	119.452	0.744	0.62
C4	Active asymmetric	Active asymmetric	32.649	44.703	41.928	119.281	0.915	0.76

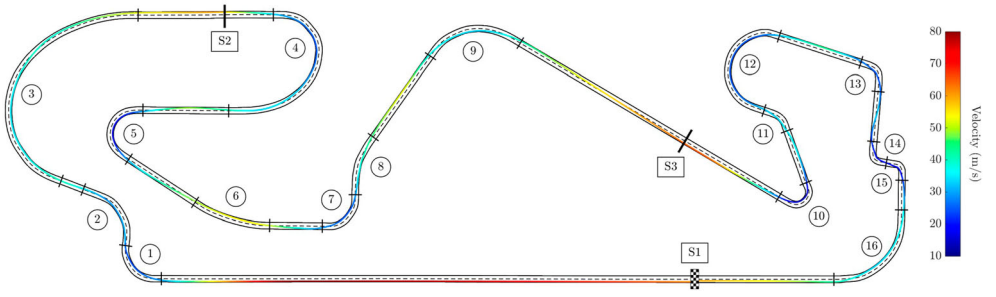

Figure 9. Optimal racing line with velocity contours for configuration 1 on the Circuit de Barcelona-Catalunya, featuring labelled sectors and corners, including corner start and end point markings.

scenarios can provide substantial performance gains. To support subsequent analyses of the impact of active aerodynamic systems on vehicle performance, the circuit's corners are categorised into low-speed, medium-speed, and high-speed, based on average cornering velocities, with the 33rd and 66th percentiles used as thresholds. Corners 5, 10, 13, 14, and 15 are classified as low-speed, with an average cornering velocity of 20.62 m/s. Corners 1, 2, 4, 7, 11, and 12 are categorised as medium-speed, averaging 28.39 m/s, while corners 3, 6, 8, 9, and 16 are identified as high-speed, with an average velocity of 40.50 m/s.

Insights into the overall performance differences between the vehicle configurations are first drawn from the analysis of velocity, steering angle, and torque data. Generally, the active aerodynamic configurations offer velocity improvements on both the straights and corners, as shown in Figure 10(a,b). Increased corner exit velocities in longer medium-to-high-speed bends such as corners 3, 4, 9, and 16 are particularly noticeable from the high delta velocity in the latter half of these corners. Additionally, later braking in heavy-braking zones is observable, particularly evident by delta velocity peaks just before corners 1, 4, 9, and 10.

The steering angle inputs, presented in Figure 10(c), show only minor deviations between the configurations, suggesting small variations in their optimal racing lines. However, noticeably less steering input is observed in corners such as 3, 4, 5, 9, 12, and 16. This suggests that the active aerodynamic configurations offer improved grip, leading to higher steering responsiveness.

The drive and brake torque inputs, shown in Figure 10(d), further reinforce the findings above. In long bends such as corners 3, 4, 9, and 16, the active aerodynamic configurations enable earlier application of drive torque, resulting in faster corner exits. In addition, these configurations allow more average brake torque to be applied, enabling later braking in heavy-braking zones before corners 1, 4, 9, and 10, as previously identified.

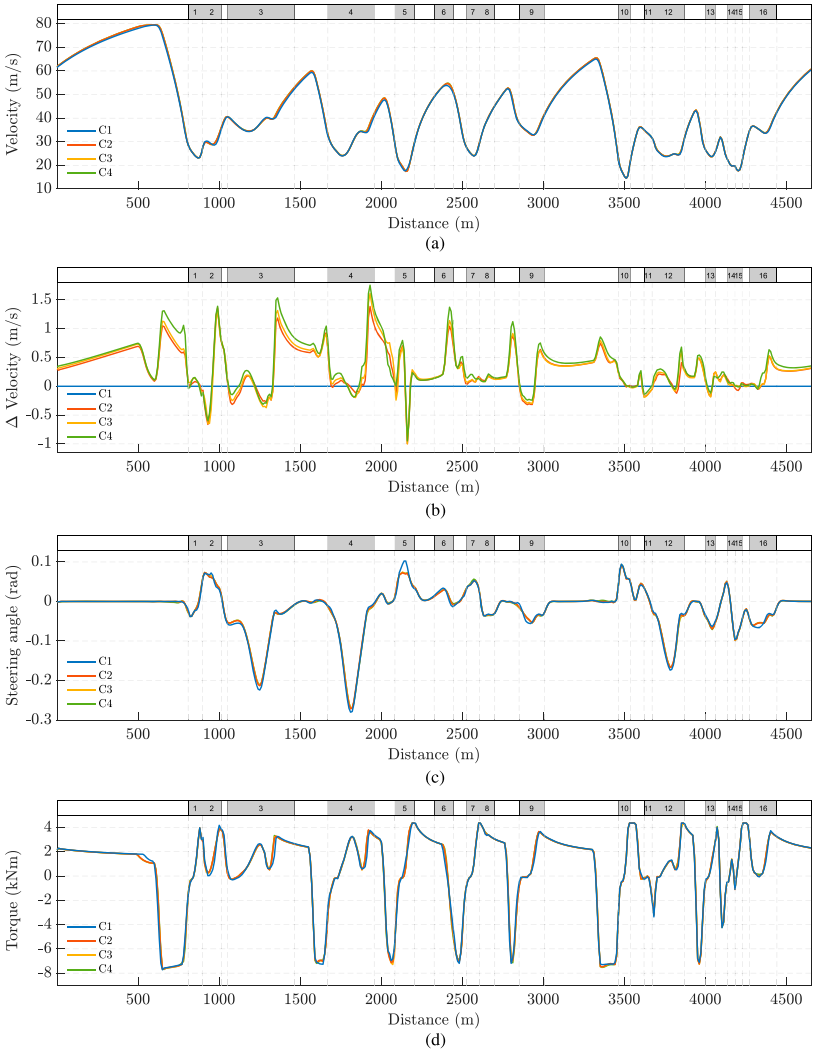

Figure 10. (a) Velocity, (b) velocity variations (c) steering angle input, and (d) total combined wheel torque as a function of distance for all vehicle configurations.

To further illustrate the performance enhancements provided by the active aerodynamic configurations, Figure 11 presents GG diagrams that map the relationship between longitudinal and lateral acceleration. In these diagrams, positive longitudinal acceleration represents forward acceleration, while negative values correspond to braking. Similarly, positive and negative lateral accelerations denote left- and right-hand cornering, respectively. The borders of each GG diagram have been highlighted to indicate the performance limits of each configuration, emphasising the operating boundaries within which the vehicle performs. Across all configurations, the diagrams show a concentration of operating points along these boundaries, demonstrating that each configuration consistently operates near its maximum potential.

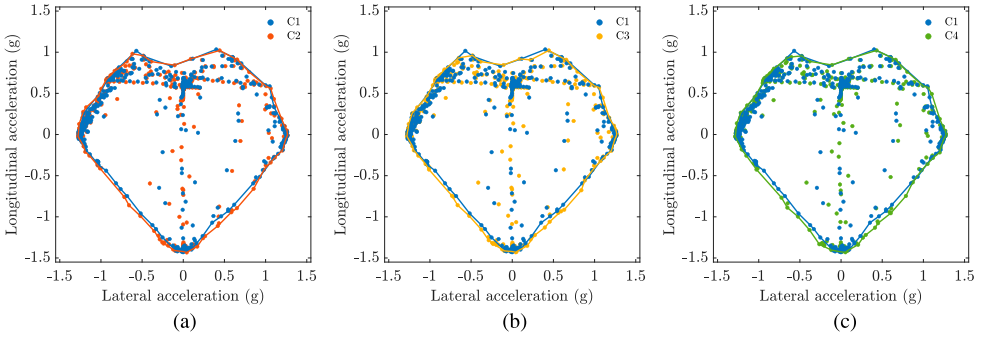

Figure 11. GG-diagrams for (a) configuration 2, (b) configuration 3, and (c) configuration 4 in comparison to configuration 1, with highlighted borders indicating the performance limits of each configuration.

The GG diagrams further confirm configuration 4 as the most capable setup, extending the performance envelope with the highest limits in both longitudinal and lateral acceleration. Relative to configuration 1, configurations 2 and 3 exhibit an approximate 2.5% increase in GG area, while configuration 4 achieves an increase of over 3.5%. In terms of pure lateral acceleration, configurations 2 and 3 show a modest improvement of less than 0.5%, whereas configuration 4 reaches nearly 1% higher lateral acceleration compared to configuration 1.

Configuration 4 also demonstrates the greatest improvements in combined deceleration and lateral acceleration in the lower quadrants of the GG diagrams, representing trail braking scenarios. Here, configurations 2 and 3 achieve an average 4.2% increase in combined acceleration, while configuration 4 sees a further improvement to 5.2% relative to configuration 1. In contrast, combined lateral and forward acceleration in the upper quadrants of the GG diagrams, which corresponds to acceleration out of corners, shows a more modest increase of less than 0.5% for configurations 2 and 3, and nearly 3% for configuration 4. These results highlight the greater overall performance gains of configuration 4, particularly in scenarios involving combined acceleration.

6.3. Optimal aerodynamic systems control

With the key performance gains identified for the active aerodynamic configurations, the analysis now evaluates the optimal control inputs for the active aerodynamic systems that drive these enhancements, as shown in Figure 12. This figure also presents longitudinal and lateral load transfer data, factors that play a crucial role in the optimal control of the aerodynamic systems.

For configuration 2, the rear wing angle is typically maximised in low-speed corners to enhance downforce and improve cornering performance, as depicted in Figure 12(a). In medium-speed corners, the angle varies between medium and high, while in high-speed corners, it ranges from low to medium. This strategy is attributed to the quadratic relationship between aerodynamic forces and velocity, achieving necessary downforce at lower angles of attack at higher speeds. Overall, the rear wing control shows notable similarities to an inverse relationship with longitudinal load transfer, increasing the angle under forward load transfer during braking and decreasing the angle under rearward load transfer during

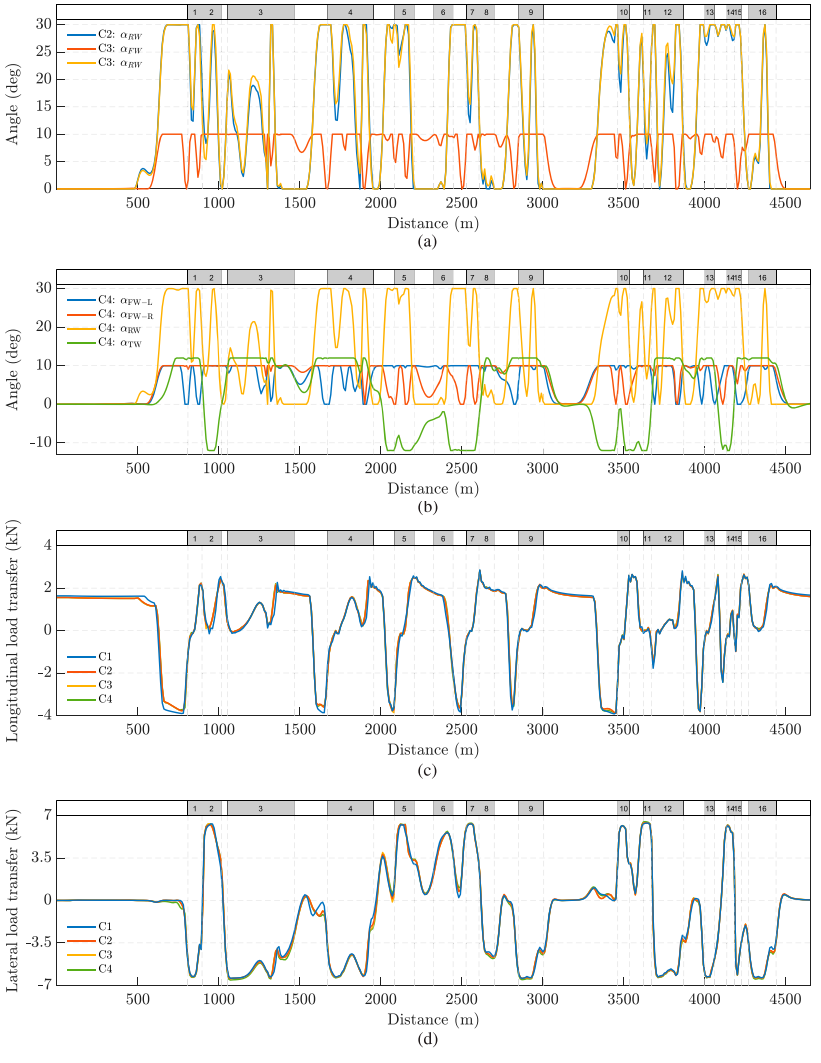

Figure 12. Optimal control of the aerodynamic systems of (a) configuration 2 and 3, (b) configuration 4, and the results of (c) longitudinal load transfer and (d) lateral load transfer as functions of distance for all vehicle configurations.

acceleration. High angles of attack during braking not only aid deceleration by increasing aerodynamic drag, but also by enhancing rear axle load, allowing the rear tyres to contribute more effectively to braking. Conversely, lowering the angle during sustained acceleration reduces aerodynamic drag, and avoids excessive rear axle loading and front axle unloading. Additionally, on straights, the rear wing is set to its minimum angle to reduce aerodynamic drag and rolling resistance, maximising straight-line speed.

The rear wing control for configuration 3, demonstrated in Figure 12(a), largely mirrors that of configuration 2, with minor adjustments to account for the active front wing's influence on the aerodynamic balance. The front wing angle is typically maximised under high lateral load transfer during cornering to increase downforce on the front axle, thereby

enhancing tyre grip and cornering performance. In heavy-braking zones, when forward load transfer peaks, the front wing angle is reduced to improve load balance, ensuring both front and rear tyres contribute effectively to deceleration. Adjustments to the front wing are less frequent compared to the rear wing, due to the rear wing's greater trade-off between downforce and drag. Front wing angle adjustments generally occur only when the rear wing is at its maximum angle, and vice versa, reflecting a coordinated approach in which the wings manage axle-specific downforce requirements in response to load shifts during acceleration, braking, and cornering. On straights, both front and rear wing angles are reduced to minimise drag and rolling resistance, maximising straight-line speed.

Configuration 4's control strategy, shown in Figure 12(b), optimises the independent left and right front wing elements, along with the adjustable rear wing angle of attack and tilt angle, providing the highest adaptability to diverse driving scenarios. During trail braking, as the vehicle initiates cornering, peak forward load transfer starts to diminish while lateral load transfer increases with steering angle application. In this phase, the inside front wing element angle is maximised to enhance grip on the less loaded front inside tyre, while the outside front wing angle is reduced to prevent further unloading of the rear axle. The rear wing angle of attack remains at its maximum to enhance rear axle load and increase aerodynamic drag, aiding deceleration. Concurrently, the rear wing maximally tilts away from the corner centre, providing a lateral force at the rear axle and a favourable downforce distribution for the inside tyres. This strategy consistently emerges at the end of braking zones, when approaching corner entry.

As the vehicle transitions from trail braking to pure cornering, where lateral load transfer predominates, both front wing elements are set to their maximum angle to enhance front axle grip. The rear wing angle of attack typically varies between low and medium levels depending on cornering speed to maintain aerodynamic balance, while the rear wing tilt remains maximised away from the corner. The tilt angle control closely mirrors the lateral load transfer patterns, generating a side force that supports lateral forces at the rear axle and enhances downforce on the inside tyres, which become underloaded with increasing lateral load transfer. This coordinated control strategy is particularly evident in longer medium-to-high-speed corners, such as corners 3, 4, 9, 11, 12, and 16.

During the initial acceleration phase when exiting a corner, lateral load transfer starts to reduce as steering input lessens, with a minor rearward load transfer occurring as initial drive torque is applied. In this phase, the inside front wing element is maximised to enhance downforce on the underloaded inside front tyre, while the outside front wing element is minimised to prevent rear axle unloading. Simultaneously, the rear wing angle of attack and tilt angle are maximised to increase downforce on the rear axle and underloaded inside tyres. This configuration effectively distributes downforce across the axles to maximise the four-wheel drive system, with the rear axle bearing most load to accommodate the majority of initial drive torque, while sufficient load remains on the front wheels for effective utilisation of the torque directed to the front wheels.

This configuration remains only briefly, as rearward load transfer intensifies and lateral load transfer decreases further during corner exit. In this phase, both front wing elements are set to their maximum angle to increase downforce on the underloaded front axle. Simultaneously, the rear wing angle of attack is minimised to prevent rear axle overloading and mitigate front axle unloading, thereby balancing the rearward load transfer. The rear wing tilt remains maximised while lateral load transfer persists, until the vehicle exits

the corner fully and enters a straight. At this point, all aerodynamic angles are set to zero, minimising drag, rolling resistance, and side forces, to maximise straight-line speed.

6.4. Vehicle design parameters

The optimal vehicle design parameters for brake, torque, and roll stiffness distributions, listed in Table 7, vary noticeably with different aerodynamic configurations. The optimal brake balance shifts progressively rearward with increasing aerodynamic control, as the active aerodynamic configurations offer improved grip at the rear tyres during braking. Configuration 1, with a high front wing angle and moderately low rear wing angle, generates limited rear axle downforce, resulting in the most front-biased brake balance. Configuration 2's active rear wing control enhances rear axle downforce during braking, resulting in a nearly 1.4% rearward shift of the optimal brake balance. In addition to the rear wing's high downforce, configuration 3 reduces its front wing angle near peak deceleration to mitigate rear axle unloading, contributing to a rearward brake balance shift of over 1.6%. Configuration 4 exhibits the highest rearward brake balance shift of over 1.7%, due to effective balancing of downforce during trail braking, further improving the braking capacity of the rear tyres.

The optimal torque distribution also shifts rearward for the active aerodynamic configurations, varying between approximately 1.6% to 1.9%. Maximising the rear wing and reducing the front wing angle during initial torque application increases downforce and traction at the rear tyres compared to configuration 1. This enhanced grip allows more torque to be applied to the rear wheels, thereby increasing the optimal torque allocation to the rear axle.

The optimal roll stiffness distribution shifts rearward for active aerodynamic configurations as well. Configurations 2 and 3 can enhance rear axle downforce during cornering compared to configuration 1, allowing greater lateral load transfer at the rear axle, resulting in a 1.7% to 2.1% rearward shift in the optimal roll stiffness distribution. Configuration 4 shows the most pronounced shift, approximately 2.7% relative to configuration 1, due to its asymmetric aerodynamic control. Its aerodynamic elements can increase downforce on the underloaded inside tyres and generate an aerodynamic side force near the rear axle during cornering, allowing configuration 4 to accommodate the highest lateral load transfer at the rear axle.

Table 7. Optimal vehicle design parameters of brake balance, torque distribution, and roll stiffness distribution for all vehicle configurations.

Configuration	Brake balance γ_b (-)	Torque distribution γ_T (-)	Roll stiffness distribution γ_{k_ϕ} (-)
C1	0.677	0.727	0.462
C2	0.667	0.739	0.470
C3	0.666	0.741	0.472
C4	0.665	0.740	0.475

7. Conclusion

This study investigated the impact of advanced active aerodynamic systems on high-performance vehicles by analysing how different aerodynamic configurations influence lap

time, driver inputs, and optimal design parameters. Specifically, the study compared static and active aerodynamic setups, with symmetric and asymmetric control of front and rear wings, investigating both the extent of performance gains and the mechanisms by which these gains are achieved.

Vehicle performance was optimised and evaluated for a lap around the Circuit de Barcelona-Catalunya using a minimum lap time simulation framework. The simulations employed a transient vehicle dynamics model based on a double-track model that incorporated longitudinal and lateral load transfer, non-linear tyre characteristics, and aerodynamic forces, obtained through RANS-based CFD simulations.

The results demonstrated that active aerodynamic configurations significantly reduce lap times compared to a static setup, with key performance improvements in braking capability, cornering speed, acceleration out of corners, and straight-line velocity. The fully active asymmetric configuration provided the highest lap time reduction of approximately 0.915 s (0.76%), as its ability to modulate downforce asymmetrically improved tyre grip utilisation, enabling the vehicle to sustain higher longitudinal and lateral accelerations.

Optimal control strategies for each configuration revealed that performance gains were achieved by actuating aerodynamic elements to balance shifts in vertical tyre loads induced by load transfer. Configurations with control over either the rear wing or both wings showed a response that correlated inversely with longitudinal load transfer, adjusting wing angles to support the underloaded axle. The configuration with fully asymmetric control capabilities was able to further maximise downforce on the underloaded inside tyres during high lateral load transfer and prioritise downforce on the most underloaded tyres in scenarios with combined load transfers.

Additionally, optimal design parameters for brake, torque and roll stiffness distributions shifted progressively rearward for the active aerodynamic configurations. These rearward shifts reflected the enhanced control over aerodynamic loads on the rear axle, enabling more effective utilisation of the rear tyres during braking, initial acceleration, and cornering.

Overall, this research demonstrated the substantial potential of active aerodynamic systems, particularly with asymmetric control, to enhance vehicle performance. The findings provided valuable insights into the extent and areas of performance improvements, the aerodynamic control strategies that drive these gains, and the resulting shifts in key vehicle design parameters. The study presented an effective simulation framework for evaluating aerodynamic control strategies and informing vehicle setup decisions, establishing a foundation for future research on advanced active aerodynamic technologies. Future work exploring control strategy implementations, integration with other active vehicle systems, and real-world applications could lead to new insights and potentially even greater performance gains, guiding the development of next-generation high-performance and automotive vehicles.

Disclosure statement

No potential conflict of interest was reported by the author(s).

Data availability statement

The minimum lap time simulation framework and the corresponding generated performance data supporting this study are openly available from Cranfield Online Research Data at: https://doi.org/10.57996/cran.ceres-2742 [47].

ORCID

Steven Rijns http://orcid.org/0000-0002-0760-2341
Tom-Robin Teschner http://orcid.org/0000-0002-6436-6197
Kim Blackburn http://orcid.org/0000-0001-8179-6132
Efstathios Siampis http://orcid.org/0000-0003-2727-8339
James Brighton http://orcid.org/0000-0001-8182-6979

References

[1] Fédération Internationale de l'Automobile. FIA 2026 F1 Regulations: SECTION C: TECHNICAL REGULATIONS. Issue 9, Published 17/10/2024.
[2] Forbes DC, Page GJ, Passmore MA, et al. A fully coupled, 6 degree-of-freedom, aerodynamic and vehicle handling crosswind simulation using the drivaer model. SAE Int J Passenger Cars – Mech Syst. 2016;9(2):710–722. doi: 10.4271/2016-01-1601
[3] Winkler N, Drugge L, Trigell AS, et al. Coupling aerodynamics to vehicle dynamics in transient crosswinds including a driver model. Comput Fluids. 2016;138:26–34. doi: 10.1016/j.compfluid.2016.08.006
[4] Nakashima T, Tsubokura M, Vázquez M, et al. Coupled analysis of unsteady aerodynamics and vehicle motion of a road vehicle in windy conditions. Comput Fluids. 2013;80:1–9. doi: 10.1016/j.compfluid.2012.09.028
[5] Carbonne L, Winkler N, Efraimsson G. Use of full coupling of aerodynamics and vehicle dynamics for numerical simulation of the crosswind stability of ground vehicles. Commer Veh. 2016;9(2):359–370.
[6] Ahangarnejad AH, Melzi S. Numerical analysis of the influence of an actively controlled spoiler on the handling of a sports car. J Vibr Control. 2018;24(22):5437–5448. doi: 10.1177/1077546318754683
[7] Mashrouteh S, Khajepour A, Kasaiezadeh A, et al. Multi-actuation controller for performance vehicles: optimal torque allocation and active aerodynamic. IEEE Trans Vehicular Technol. 2022;71(3):2721–2733. doi: 10.1109/TVT.2022.3144133
[8] Ferraris A, De Cupis D, Pinheiro HC, et al. Integrated design and control of active aerodynamic features for high performance electric vehicles. In: 2020 SAE Brasil Congress & Exhibition; Soa Paulo, Brazil. SAE International; 2021.
[9] Broniszewski J, Piechna J. A fully coupled analysis of unsteady aerodynamics impact on vehicle dynamics during braking. Eng Appl Comput Fluid Mech. 2019;13(1):623–641.
[10] Broniszewski J, Piechna J. Fluid-structure interaction analysis of a competitive car during brake-in-turn manoeuvre. Energies. 2022;15(8):2917. doi: 10.3390/en15082917
[11] Kurec K, Remer M, Piechna J. The influence of different aerodynamic setups on enhancing a sports car's braking. Int J Mech Sci. 2019;164:105140. doi: 10.1016/j.ijmecsci.2019.105140
[12] Ayyagari DT, He Y. Aerodynamic analysis of an active rear split spoiler for improving lateral stability of high-speed vehicles. Int J Vehicle Syst Modell Testing. 2017;12(3-4):217–239. doi: 10.1504/IJVSMT.2017.089978
[13] Sikder T, Kapoor S, He Y. Optimizing dynamic performance of high-speed road vehicles using aerodynamic aids. In: Proceedings of the ASME 2016 International Mechanical Engineering Congress and Exposition. Volume 7: Fluids Engineering; November 11–17; Phoenix, Arizona, USA. ASME; 2016. p. V007T09A060. doi: 10.1115/IMECE2016-65414

[14] Hammad M, Qureshi K, He Y. Safety and lateral dynamics improvement of a race car using active rear wing control. In: WCX SAE World Congress Experience; Detroit, Michigan, USA. SAE International; 2019.
[15] van Aaken JPT. Influence of asymmetric aerodynamics on lateral acceleration on a formula student car [B.sc thesis]. Department of Mechanical Engineering, Eindhoven University of Technology; 2023.
[16] Cai J, Kapoor S, Sikder T, et al. Effects of active aerodynamic wings on handling performance of high-speed vehicles. In: WCX 17: SAE World Congress Experience; Detroit, Michigan, USA. SAE International; 2017.
[17] Diba F, Barari A, Esmailzadeh E. Handling and safety enhancement of race cars using active aerodynamic systems. Veh Syst Dyn. 2014;52(9):1171–1190. doi: 10.1080/00423114.2014.930158
[18] Zavala D, Vicente W, Esquivel R, et al. Numerical simulation of the effect of a centripetal wing spoiler on the flow aerodynamics of a sports car. SAE Technical Paper 2023-01-5032, 2023.
[19] Piechna JR, Kurec K, Broniszewski J, et al. Influence of the car movable aerodynamic elements on fast road car cornering. Energies. 2022;15(3):689. doi: 10.3390/en15030689
[20] Rijns S, Teschner T-R, Blackburn K, et al. Performance analyses of active aerodynamic load balancing designs on high-performance vehicles in cornering conditions. Phys Fluids. 2024;36(8):085199. doi: 10.1063/5.0222780
[21] Casanova D. On minimum time vehicle manoeuvring: the theoretical optimal lap [dissertation]. School of Mechanical Engineering, Cranfield University; 2000.
[22] Massaro M, Limebeer DJN. Minimum-lap-time optimisation and simulation. Veh Syst Dyn. 2021;59(7):1069–1113. doi: 10.1080/00423114.2021.1910718
[23] Veneri M, Massaro M. A free-trajectory quasi-steady-state optimal-control method for minimum lap-time of race vehicles. Veh Syst Dyn. 2020;58(6):933–954. doi: 10.1080/00423114.2019.1608364
[24] Lovato S, Massaro M. Three-dimensional fixed-trajectory approaches to the minimum-lap time of road vehicles. Veh Syst Dyn. 2022;60(11):3650–3667. doi: 10.1080/00423114.2021.1969024
[25] Lovato S, Massaro M. A three-dimensional free-trajectory quasi-steady-state optimal-control method for minimum-lap-time of race vehicles. Veh Syst Dyn. 2022;60(5):1512–1530. doi: 10.1080/00423114.2021.1878242
[26] Warren E, Limebeer DJN, Bastin M, et al. Optimal control of a nascar – specification race car. Veh Syst Dyn. 2023;61(5):1210–1235. doi: 10.1080/00423114.2022.2067573
[27] Christ F, Wischnewski A, Heilmeier A, et al. Time-optimal trajectory planning for a race car considering variable tyre-road friction coefficients. Veh Syst Dyn. 2021;59(4):588–612. doi: 10.1080/00423114.2019.1704804
[28] Perantoni G, Limebeer DJN. Optimal control for a formula one car with variable parameters. Veh Syst Dyn. 2014;52(5):653–678. doi: 10.1080/00423114.2014.889315
[29] Masouleh MI, Limebeer DJN. Optimizing the aero-suspension interactions in a formula one car. IEEE Trans Control Syst Technol. 2016;24(3):912–927. doi: 10.1109/TCST.2015.2475396
[30] Jiménez Elbal A, Conde AZ, Siampis E. Simultaneous optimisation of vehicle design and control for improving vehicle performance and energy efficiency using an open source minimum lap time simulation framework. World Electric Veh J. 2024;15(8):366. doi: 10.3390/wevj15080366
[31] de Buck P, Martins JRRA. Minimum lap time trajectory optimisation of performance vehicles with four-wheel drive and active aerodynamic control. Veh Syst Dyn. 2023;61(8):2103–2119. doi: 10.1080/00423114.2022.2101930
[32] Soares RF, Knowles A, Olives SG, et al. On the aerodynamics of an enclosed-wheel racing car: an assessment and proposal of add-on devices for a fourth, high-performance configuration of the drivaer model; 2018. SAE Technical Paper 2018-01-0725.
[33] Heft A, Indinger T, Adams N. Introduction of a new realistic generic car model for aerodynamic investigations. SAE Technical Paper 2012-01-0168, 2012.

[34] Rijns S, Teschner T-R, Blackburn K, et al. Effects of cornering conditions on the aerodynamic characteristics of a high-performance vehicle and its rear wing. Phys Fluids. 2024;36(4):045119. doi: 10.1063/5.0204204
[35] Rijns S, Teschner T-R, Blackburn K, et al. Integrated numerical and experimental workflow for high-performance vehicle aerodynamics. SAE Technical Paper 2024-01-5016, 2024. doi: 10.4271/2024-01-5016
[36] Rijns S, Teschner T-R, Blackburn K, et al. Aerodynamic analysis of the ride height dependency of a high-performance vehicle equipped with a multichannel diffuser in ground effect. SAE Technical Paper 2023-01-5064, 2023. doi: 10.4271/2023-01-5064
[37] Rijns S, Teschner T-R, Blackburn K, et al. Experimental and numerical investigation of the aerodynamic characteristics of high-performance vehicle configurations under yaw conditions. Phys Fluids. 2024;36(4):045112. doi: 10.1063/5.0196979
[38] Lanfrit M. Best practice guidelines for handling automotive external aerodynamics with fluent. Fluent Deutschland GmbH; 2005.
[39] Saunders JW, Ben Mansour R. On-road and wind tunnel turbulence and its measurement using a four-hole dynamic probe ahead of several cars. In: SAE 2000 World Congress; Detroit, Michigan, USA. SAE International; 2000.
[40] Modeling turbulent flows – introductory fluent training, [accessed 2006 May 01]. https://www.southampton.ac.uk/ nwb/lectures/GoodPracticeCFD/Articles/Turbulence_Notes_Fluent-v6.3.06.pdf.
[41] Menter FR. Two-equation eddy-viscosity turbulence models for engineering applications. Aiaa J. 1994;32(8):1598–1605. doi: 10.2514/3.12149
[42] Purdy DJ, Velenis E, Assadian F, et al. Optimal control of motorsport differentials. Veh Syst Dyn. 2015;53(12):1772–1794. doi: 10.1080/00423114.2015.1093150
[43] Dixon JC. Tires, suspension and handling. 2nd ed. Warrendale (PA): SAE International; 1996.
[44] Pacejka HB. Tire and vehicle dynamics. 3rd ed. Oxford: Butterworth-Heinemann; 2012.
[45] Tyres A. Technical data resources [accessed 2024 Apr 12]; 2024.
[46] Helix. SPM242-176 electric motor unit specification sheet [accessed 2024 Aug 11]; 2024.
[47] Rijns S, Siampis E, Teschner T-R, et al. Minimum lap time simulation framework: active aerodynamics and torque distribution; 2025. doi: 10.57996/cran.ceres-2742

Optimising vehicle performance with advanced active aerodynamic systems

Rijns, Steven

2025-12-31

Rijns S, Teschner T-R, Blackburn K, et al., (2025) Optimising vehicle performance with advanced active aerodynamic systems. Vehicle System Dynamics, Available online 14 May 2025 https://doi.org/10.1080/00423114.2025.2505619